

Clustering of quasars in SDSS-IV eBOSS : study of potential systematics and bias determination.

**Pierre Laurent,^a Sarah Eftekharzadeh,^b Jean-Marc Le Goff,^{a,1}
Adam Myers,^b Etienne Burtin,^a Martin White,^{c,d,e} Ashley Ross,^f
Jeremy Tinker,^g Rita Tojeiro,^h Julian Bautista,ⁱ Johan Comparat,^j
Hélion du Mas des Bourboux,^a Jean-Paul Kneib,^k Ian D.
McGreer,^l Nathalie Palanque-Delabrouille,^a Will J. Percival,^m
Francisco Prada,ⁿ Graziano Rossi,^o Donald P. Schneider,^p
Micheal Strauss,^q David Weinberg,^r Christophe Yèche,^a Pauline
Zarrouk,^a and Gong-Bo Zhao^s**

^aCEA, Centre de Saclay, IRFU/SPP, F-91191 Gif-sur-Yvette, France

^bDepartment of Physics and Astronomy, University of Wyoming, Laramie, WY 82071, USA

^cLawrence Berkeley National Lab, 1 Cyclotron Rd, Berkeley CA 94720, USA

^dDepartment of Physics, University of California, Berkeley, CA 94720, USA

^eDepartment of Astronomy, University of California, Berkeley, CA 94720, USA

^fDepartment of Astronomy, The Ohio State University, Columbus, OH 43210, USA

^gCenter for Cosmology and Particle Physics, Department of Physics, New York University, New York, 10003, USA

^hSchool of Physics and Astronomy, North Haugh, St. Andrews KY16 9SS, UK

ⁱDepartment of Physics and Astronomy, University of Utah, Salt Lake City, UT 84112, USA

^jMax-Planck-Institut für Extraterrestrische Physik, Giessenbachstraße, 85748 Garching, Germany

^kLaboratoire d'Astrophysique, École Polytechnique Fédérale de Lausanne, 1015 Lausanne, Switzerland

^lSteward Observatory, University of Arizona, Tucson, AZ 85721-0065, USA

^mInstitute of Cosmology and Gravitation, University of Portsmouth, Dennis Sciama building, PO1 3FX, Portsmouth, UK

ⁿInstituto de Física Teórica (IFT) UAM/CSIC, Universidad Autónoma de Madrid, Cantoblanco, E-28049 Madrid, Spain

^oDepartment of Astronomy and Space Science, Sejong University, Seoul, 143-747, Korea

^pInstitute for Gravitation and the Cosmos, Pennsylvania State University, University Park, PA 16802, USA

^qDepartment of Astrophysical Sciences, Princeton, NJ 08544, USA

¹Corresponding author.

^rDepartment of Physics and Center for Cosmology and AstroParticle Physics, The Ohio State University, Columbus, OH 43210, USA

^sNational Astronomical Observatories of China, Beijing 100012, China

E-mail: jmlegoff@cea.fr

Abstract. We study the first year of the eBOSS quasar sample in the redshift range $0.9 < z < 2.2$ which includes 68,772 homogeneously selected quasars. We show that the main source of systematics in the evaluation of the correlation function arises from inhomogeneities in the quasar target selection, particularly related to the extinction and depth of the imaging data used for targeting. We propose a weighting scheme that mitigates these systematics. We measure the quasar correlation function and provide the most accurate measurement to date of the quasar bias in this redshift range, $b_Q = 2.45 \pm 0.05$ at $\bar{z} = 1.55$, together with its evolution with redshift. We use this information to determine the minimum mass of the halo hosting the quasars and the characteristic halo mass, which we find to be both independent of redshift within statistical error. Using a recently-measured quasar-luminosity-function we also determine the quasar duty cycle. The size of this first year sample is insufficient to detect any luminosity dependence to quasar clustering and this issue should be further studied with the final $\sim 500,000$ eBOSS quasar sample.

Keywords: Large scale structure of the universe, redshift surveys, galaxy clustering

Contents

1	Introduction	2
2	Data sample	3
2.1	eBOSS survey	3
2.2	Quasar selection	4
3	Analysis	4
3.1	Computing $\xi(r)$	4
3.2	Estimation of statistical uncertainties	6
4	Systematic effects	8
4.1	Inhomogeneities of target identification	8
4.2	Inhomogeneities of quasar target selection	9
4.3	Effect of weightings on $\xi(r)$	9
5	Measurement of the quasar bias	10
6	The halo mass and the duty cycle of eBOSS quasars	12
6.1	Characteristic Halo Mass	13
6.2	Duty Cycle	15
7	Conclusion	18

1 Introduction

The best current constraints on the cosmological parameters are from the power spectrum of temperature fluctuations [e.g. 1–5] in the Cosmic Microwave Background (henceforth CMB). In this regard, the latest Planck satellite results provide overwhelming evidence for non-zero cosmic acceleration or “dark energy” with $\Omega_{\text{DE}} = 0.692 \pm 0.012$ [6]. The CMB, however, can only provide a measurement at one redshift (the epoch of the surface of last scattering at $z \sim 1100$), and, so, measurements across many redshifts are required to constrain the equation of state of dark energy [e.g. 7–9]. As galaxies and quasars occupy a three-dimensional web that traces a range of redshifts, they offer a unique probe of the evolution of dark energy over more than 10 billion years of cosmic history. Cosmological experiments are thus, increasingly, turning in part to vast redshift surveys in an attempt to map the Universe in order to specifically study dark energy through the growth of structure [e.g. 10–14].

The first significant galaxy redshift surveys [e.g. 15–17], were improved upon by surveys such as the 2dF Galaxy Redshift survey [18], the DEEP2 survey [19] and the Sloan Digital Sky Survey [henceforth SDSS; 20] “main” galaxy sample [21] and Luminous Red Galaxy (henceforth LRG) sample [22]. The use of galaxies from such surveys as tracers at significantly lower redshifts than the CMB have helped to precisely pin down our cosmological world model [e.g. 23–28]. In particular, such surveys have been used to measure the influence of baryons on galaxy clustering [29] and to confirm the potential use of baryon-driven fluctuations (so-called Baryon Acoustic Oscillations, or BAOs) in the galaxy power spectrum as a standard ruler with which to set the cosmological distance scale [30].

The realization that essentially every galaxy hosts a supermassive black hole [e.g. 31–34], and that a quasar is therefore just a phase in the normal cycle of a galaxy, prompted the more general use of quasars as cosmological tracers. Recent major redshift surveys have also, therefore, used quasars to probe large-scale structure, with the 2dF QSO Redshift Survey [35] and the Sloan Digital Sky Survey (SDSS) quasar surveys [e.g. 36, 37] being notable examples. Quasar redshift surveys have often operated in tandem with galaxy surveys, and have highlighted the possibility of using quasars to constrain cosmology at higher redshifts than would be possible for galaxy samples to similar magnitude limits [e.g. 38–40].

In addition to probing cosmology, quasar clustering can be used as a tool to constrain the interplay of supermassive black holes, galaxies, and dark matter halos, and how that interplay evolves with cosmic time. Measuring the bias of quasars constrains the mass of the dark matter halos that quasars occupy. In turn, measuring the abundance of such halos compared to the number density of the quasars they host can begin to constrain the duration of the quasar phase. In general, this has led to a consistent picture where UV/optically luminous quasars are biased by a factor of $b_{\text{Q}} \sim 2$ at redshift $z \sim 1$ rising to $b_{\text{Q}} \sim 3$ at $z \sim 2$ and $b_{\text{Q}} > 4$ at $z > 3$ [e.g. 41–49]. This implies that UV/optically luminous quasars at $z < 2.5$ are hosted by halos with an average mass of a few times $10^{12} h^{-1} M_{\odot}$ and are “on” for a few per cent of the Hubble time. Precise bias and mass measurements for UV/optically luminous quasars at multiple redshifts are crucial in helping to tie down the role of quasars in galaxy evolution [see, e.g., 50, for an overview]. In particular, by comparing such clustering measurements to quasar and star-formation signatures across the electromagnetic spectrum [e.g. 51–60].

As clustering measurements have become increasingly precise, they have become dominated by systematics. Some systematics arise from per-cent-level imperfections in calibrating the target imaging or survey spectroscopy that are critical to assembling large redshift catalogs. Other common systematics include contamination by non-cosmological sources such as stars, or general foregrounds such as Galactic dust. Such systematics can be scale-dependent, affecting not just the amplitude of clustering measurements, but also the overall shape of the power spectrum of tracers. Obviously, this

can be a concern for both cosmological constraints and for characterizing the dark matter halos occupied by tracer populations. To counter this, procedures have been developed to calculate weighting maps and exclusion masks to ameliorate clustering systematics both for galaxies [e.g 61–63] and for quasars [64–69].

The Baryon Oscillation Spectroscopic Survey [BOSS; 12] conducted as part of the third iteration of the SDSS [70] focused on using quasars and galaxies as complementary probes of a BAO feature at $\sim 100 h^{-1}$ Mpc in order to calibrate the redshift-distance relation. At redshifts of $z < 0.7$, galaxies were used as direct tracers of the matter power spectrum [e.g 71–73] and at $z > 2.1$ clouds of neutral hydrogen in the Lyman- α Forest, as illuminated by background quasar-light, were similarly used [74–78]. Beyond its cosmological impact, BOSS provided by far the most precise constraints on the bias and host-halo-masses of quasars at $z \sim 2.5$ [48, 49]. The success of BOSS led to the development of an extended spectroscopic redshift survey using the SDSS telescope [extended-BOSS or eBOSS; 14]. The cosmological goal of eBOSS [79] is to detect the $\sim 100 h^{-1}$ Mpc BAO scale in redshift ranges not yet probed by spectroscopic surveys; LRGs at $0.7 < z < 0.9$ [80]; Emission Line Galaxies at $z \sim 0.9$ [81, 82] and quasars at $0.9 < z < 3.5$ [83]. In addition eBOSS will attempt to improve BAO constraints by identifying new quasars to trace the Lyman- α Forest [84].

Ultimately, eBOSS will provide over half-a-million spectroscopically confirmed quasars at redshifts of $z > 0.9$ [83]. This sample will provide an unparalleled opportunity to study galaxy evolution and the BAO scale through quasar clustering, particularly with careful control of the systematics that can contaminate clustering measurements. In this paper, we present measurements of quasar clustering using the first year of eBOSS observations. The sample that we analyze approaches 70,000 optically luminous quasars in the redshift range $0.9 < z < 2.2$. Even after only its first year, eBOSS has spectroscopically confirmed ~ 2 – 3 times as many $0.9 < z < 2.2$ quasars as used in the main clustering analyses of the 2dF QSO Redshift Survey and the SDSS-I/II [e.g. 41, 46, 47]. In this paper, we focus on correcting for the systematics and inhomogeneities that can contaminate eBOSS clustering measurements. We measure the evolution of quasar bias with unprecedented precision. We then interpret our bias measurements in terms of the characteristic masses of quasar-hosting halos, and estimate the duty cycle of quasars at $0.9 < z < 2.2$. A companion paper [85] reexamines our analyses in the context of sophisticated N-body simulations.

2 Data sample

2.1 eBOSS survey

The six years of observations of eBOSS [14] started in July 2014. At the end of the survey a sample of more than 500,000 spectroscopically confirmed quasars will be available over 7500 deg^2 in the redshift range $0.9 < z < 2.2$. This will allow for a measurement of the BAO scale and provide measurements of the angular diameter distance, $d_A(z)$, and of $H(z)$ to a 2.8% and a 4.2% accuracy, respectively [79]. The program also includes 250,000 new luminous red galaxies (LRG) at $\langle z \rangle = 0.72$, to be combined with BOSS LRGs and 195,000 emission-line galaxies at $\langle z \rangle = 0.87$. Finally the spectra of 60,000 new quasars at $z > 2.1$ will be measured and the spectra of 60,000 known quasars at $z > 2.1$ will be remeasured to improve their signal-to-noise ratio. This will improve BOSS Lyman- α BAO measurement.

The program makes use of upgraded versions of the SDSS spectrographs [86] mounted on the Sloan 2.5-meter telescope [87] at Apache Point Observatory, New Mexico. An aluminum plate is set at the focal plane of the telescope with a 3° diameter field-of-view. Holes are drilled in the plate, corresponding to 1000 targets, i.e., objects to be observed with one of the two spectrographs. An optical fiber is plugged to each hole and links to the spectrographs. The minimum distance between

two fibers on the same plate corresponds to 62” on the sky, which results in some “collisions” between targets. It may, however, be possible to observe both colliding targets if they are in the overlap region between two or more plates.

2.2 Quasar selection

The eBOSS quasar selection [83] involves a homogeneous CORE selection that combines an optical selection in (u, g, r, i, z) bands, using a likelihood-based routine called XDQSOz, with a mid-IR-optical color cut. The extreme deconvolution (XD) algorithm¹ was applied in BOSS to model the distributions of quasars and stars in flux space, and hence to separate quasar targets from stellar contaminants [XDQSO; 89]. In eBOSS we use the XDQSOz extension [90], which selects quasars in any specified redshift range. We start from the SDSS photometric images in 5 bands (u, g, r, i, z) [91] with updated calibration of SDSS imaging relative to BOSS [92]. We select point sources with deextincted PSF magnitudes $g < 22$ or $r < 22$ that have an XDQSOz probability $P(z > 0.9) > 0.2$. This selection includes quasars at $z > 2.2$, which are not used for direct quasar clustering but for Lyman- α forest studies. There is another quasar selection in eBOSS dedicated to $z > 2.2$ Lyman- α quasars, with an average 20 targets per deg². We do not discuss it here.

In contrast to quasars, stars tends to be dim in the mid-IR wavelengths. We make a weighted average of the WISE [93] $w1$ and $w2$ mid-IR fluxes to optimize the S/N ratio and similarly a weighted average of SDSS g , r and i PSF fluxes. Selecting targets with a resulting average optical magnitude significantly larger than the IR magnitude such that $m_{\text{opt}} - m_{\text{IR}} \geq (g - i) + 3$, reduces the star contamination in our sample without significantly removing quasars.

This selection results in an average 115 targets per deg², out of which 25 have already been observed by SDSS I, II or III, so there remain 90 targets per deg² to be measured by eBOSS. These 25 and 90 targets per deg² result, respectively, in 13 quasars per deg² that we call “known quasars” and 58 new quasars per deg² that we call “eBOSS quasars”, in both case in the range $0.9 < z < 2.2$. This makes a total of about 70 quasars per deg² and matches the requirement to reach a 2% accuracy on the BAO scale [14].

Part of the eBOSS footprint was observed by SEQUELS [14, 83], a pilot survey at the end of SDSS III. SEQUELS differs from the rest of eBOSS survey in two ways: the apatial placement of the plates was denser, one plate per ≈ 4 deg² instead of one plate per ≈ 5 deg², and all quasar-target spectra were visually inspected. The first difference is taken into account by the completeness (see section 3.1) and, in order to treat them as all eBOSS quasars, we use only the pipeline information for SEQUELS quasars.

The data used in this paper include all spectra taken during the first year of eBOSS data taking, up to July 2015. They cover a surface of 1200 deg².

3 Analysis

3.1 Computing $\xi(r)$

There are a limited number of fibers available so all targets cannot be ascribed a fiber and observed. Since the density of eBOSS targets is not homogeneous, their probability to be observed is not homogeneous either. In addition targets are more likely to be observed when located on areas where plates overlap. In order to take those effects into account we define polygons as the intersections of

¹XD [88] is a method to describe the underlying distribution function of a series of points in parameter space (e.g., quasars in color space) by modeling that distribution as a sum of Gaussians convolved with measurement errors.

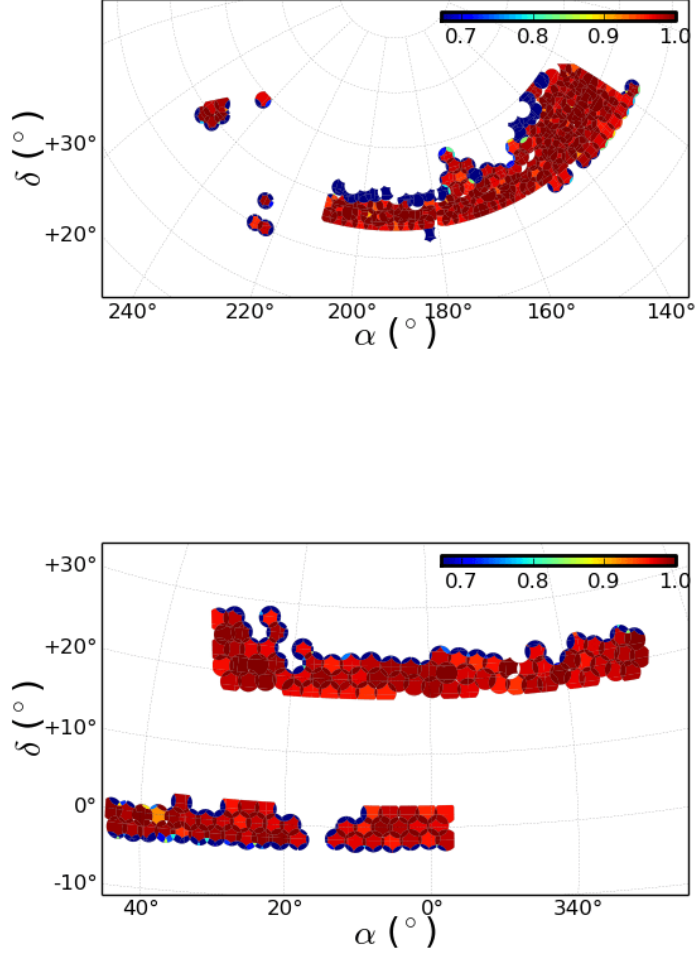


Figure 1. Angular distribution of the selected data in the NGC (left) and the SGC (right). The color scale indicates the survey completeness in each polygon.

the plates projected on the celestial sphere, and in each polygon we define a completeness

$$C = \frac{N_{\text{obs}} + N_{\text{col}}}{N_{\text{targets}} - N_{\text{known}}}. \quad (3.1)$$

Here N_{obs} is the number of observed targets, N_{targets} the total number of targets, N_{known} the number of targets that have already been observed by the SDSS I, II and BOSS surveys, and N_{col} is the number of targets that were not observed because they are colliding with a quasar. Known targets are not re-observed by eBOSS in order to save fibers, and are thus removed from the denominator of equation 3.1. Besides, known target completeness is by definition equal to 1, which would bias our measurement. In order to force the known-target completeness to be the same as for other targets, we remove some known targets from the sample with a survival probability equal to the value of the

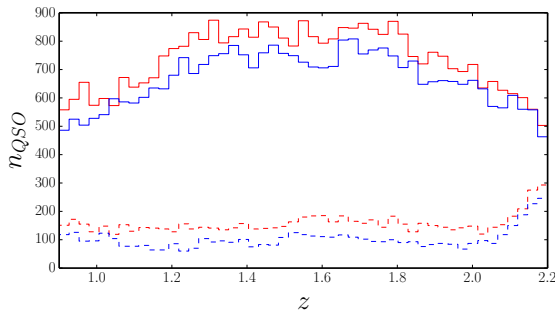


Figure 2. Redshift distribution of eBOSS quasars (continuous line) and known quasars (dashed line) in the NGC (red) and SGC (blue).

completeness in their polygon. We account for collisions as in Anderson et al. [94]: when a target is not observed due to collision, we upweight by one unit the closest observed quasar within $62''$ (for limitations of this approach, see Bianchi and Percival [95]). Therefore we add these collided targets to the numerator when computing the completeness. If there is no quasar within $62''$, this target is treated as any other unobserved targets. Figure 1 shows the completeness of the eBOSS survey in the North Galactic Cap (NGC) and South Galactic Cap (SGC), as computed with the Mangle software [96].

To correct for completeness, we generate a catalog of 10^7 objects with “random” angular positions over the eBOSS footprint, with the number of random objects in each polygon proportional to its area times its completeness. We then assign to each random object a redshift that is drawn from the measured redshift distribution $n(z)$, see Figure 2. Finally, we compute $\xi(r)$ with the Landy-Szalay estimator [97]:

$$\hat{\xi}^{\text{LS}}(r) = \frac{dd(r) - 2dr(r) + rr(r)}{rr(r)}, \quad (3.2)$$

where $dd(r)$ is the number of pairs of quasars separated by a distance r , $dr(r)$ is the number of pairs between a quasar and an object from the random catalog, and $rr(r)$ the number of pairs of random objects. These three quantities are normalized to the total number of pairs.

As mentioned in section 2, the measure of the correlation function $\xi(r)$ is very sensitive to inhomogeneities in the quasar target selection. We apply masks to remove from our sample all quasars and random objects that are located in areas where the target selection is too contaminated to be modelled and easily corrected. These areas include regions around bright objects (stars or galaxies) and where the SDSS photometry is unreliable. We also remove areas covered by the centerpost of the eBOSS plates, since we cannot observe those areas.

3.2 Estimation of statistical uncertainties

We compare two methods to compute covariance matrices. The first method, developed by Laurent et al. [69], uses bootstrap realizations. For each galactic cap, we define 201 bootstrap cells. We obtain a bootstrap realization by drawing 201 cells with replacement from the 201 bootstrap cells, and compute $\xi(r)$ for this realization. We repeat this operation 10,000 times, and estimate the covariance matrix of $\xi(r)$ from the covariance of $\xi(r)$ for these 10,000 realizations. Bootstrap resampling ignores cosmic variance, but this is not an issue here since our sample is shot-noise limited. Finally, we note

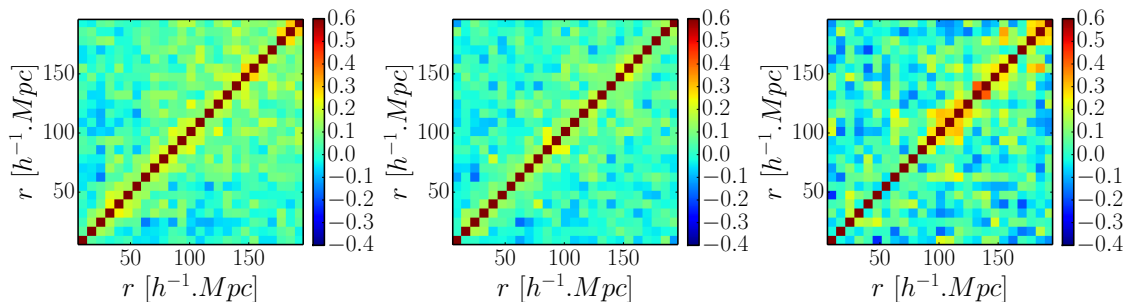


Figure 3. Correlation matrices of $\xi(r)$ computed using bootstrap realizations without systematic weighting (left), with systematic weighting (center), and using QPM mocks (right).

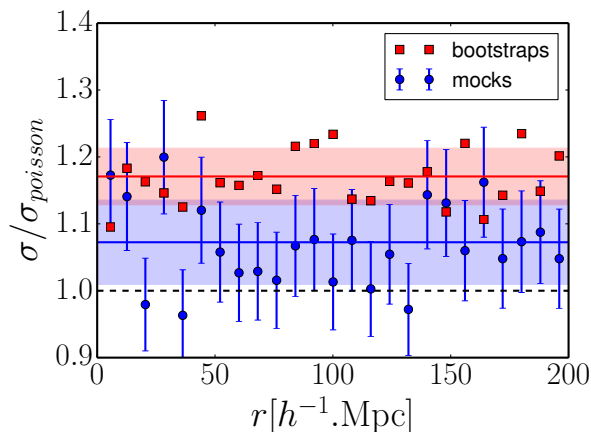


Figure 4. Ratio of bootstrap errors to Poisson errors (red squares) and, ratio of mock errors to Poisson errors (blue dots). The lines correspond to the mean value of the ratio, and the bands represent the rms of the dots.

that computing the covariance matrix from data resampling means that it includes variations caused by systematic effects present in the data.

We also compute covariance matrices using 100 QPM mocks [98] for each galactic cap. These mocks take into account cosmic variance, but they struggle to model the correlation function on small scales. However, this is not problematic because these scales are not relevant for this study.

Figure 3 displays the correlation matrices of $\xi(r)$ for the full eBOSS survey obtained with the mocks and the bootstrap realizations. We note that systematic weighting (Section 4) slightly reduces the amplitude of the off-diagonal elements of the bootstrap correlation matrices on large scales (center compared to left). The mock correlation matrix is noisier because we only have 100 mock catalogues. Figure 4 shows the ratio of bootstrap and mock errors to Poisson errors. We see that bootstrap errors are systematically larger than mock errors, but provide a more accurate determination of uncertainties. In the following, we will always display statistical uncertainties obtained from bootstrap realizations.

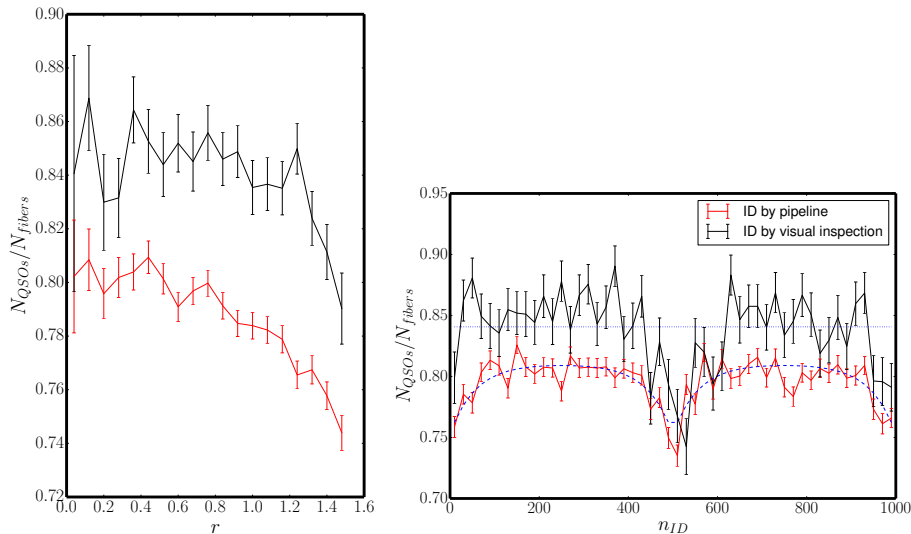


Figure 5. The N_{QSO}/N_{fibers} ratio with respect to r (left, in radians) and n_{ID} (right). The black lines correspond to the visually inspected quasar sample, the red lines correspond to the new eBOSS quasar sample, identified by the pipeline. The dashed blue line corresponds to a fit of the function in equation 4.1 on the new eBOSS quasar sample, and the dotted blue lines corresponds to a fit of a constant on the visually inspected quasar sample.

4 Systematic effects

4.1 Inhomogeneities of target identification

The SDSS I-II and BOSS surveys observed a total of 12,759 quasars within our target sample. These “known quasars” were spectroscopically identified by visual inspection [99], whereas newly observed targets are identified automatically by the eBOSS pipeline. The efficiency of target identification is known to be better for the visual inspection than for the pipeline, and such a difference can generate systematic effects. This efficiency also depends on the signal-to-noise ratio, which varies with the position of the fiber in the spectrographs. Fibers with an identifier, n_{ID} , close to 0, 500 or 1000 are located on the edges of the spectrographs, and their spectra are on average noisier than for other fibers. Since the fiber IDs are also correlated with the position of the fiber in the focal plane, the difference in noise can generate correlations at scales of the order of the plate width.

Figure 5 shows the ratio of the number of identified quasars to the number of fibers, N_{QSO}/N_{fibers} , versus the distance to the center of the plate, r , and versus the fiber ID, n_{ID} . The red lines correspond to the newly observed eBOSS targets, identified by the pipeline. The black lines correspond to the targets that have been visually inspected, including all known eBOSS quasars.

As expected, the ratio N_{QSO}/N_{fibers} is higher for visually inspected targets than for targets identified with the pipeline, and both ratios present a significant variation with respect to n_{ID} and r . The dependency with n_{ID} is well fitted by a hyperbolic cosine with 3 free parameters:

$$\frac{N_{QSO}}{N_{fibers}}(n_{ID}) = -a \cosh\left(\frac{n_{ID} \bmod 500 - 250}{b}\right)^2 + c. \quad (4.1)$$

The resulting fit corresponds to the dashed blue line of Figure 5. We correct this effect by weighting eBOSS quasars by the inverse of equation 4.1. Since we do not know the fiber number for

all known quasars, we simply weight them with the inverse of the mean value of the ratio, displayed by the blue dotted straight line on Figure 5. This takes into account the difference of efficiency of identification between known and new eBOSS quasars. Comparing blue points with magenta dots in Figure 7 shows that this unidentification weighting has little effect on $\xi(r)$. In addition we also tried a weighting scheme where the hyperbolic cosine dependency for new eBOSS quasars is replaced by the mean value of the ratio, as is done for known quasars. This showed that most of the (small) effect of the unidentification weight comes from the difference of efficiency between the two categories of targets rather than from the dependence of the weight with n_{ID} . So neglecting the dependence of the weight with n_{ID} for known quasars is safe.

4.2 Inhomogeneities of quasar target selection

Quasar targets are selected with the XDQSOz algorithm (section 2.2), which aims at providing a homogeneous target selection using the SDSS photometry. The SDSS photometry, however, is not perfectly homogeneous. The mean 5σ detection limit for a point source (also called depth) for the SDSS photometry is $g = 23.1$ and $r = 22.7$, but it varies with angular position by up to ± 0.8 magnitude (see histogram on Figure 6). Targets are selected up to a given apparent magnitude limit of $g = 22.0$ or $r = 22.0$, therefore some faint sources can end up very close to the detection limit. Uncertainties on their relative flux measurements will be significantly higher than for other sources, so the XDQSOz probability of faint sources may go below the selection threshold. Also, observed fluxes of faint sources might be biased by the fluxes of close brighter sources, an effect known as blending.

We study the variation of the observed-quasar density with the depth and its inputs (seeing, airmass, Galactic extinction and sky-flux). We also study the variation with star density, since it can bias the target selection through blending. To do so, we generate Healpix maps with $N_{\text{side}} = 256$ for each of the aforementioned quantities, following the procedure of *Ross et al. 2012* [62]. We also create a map for the ratio of the number of observed quasars to the normalized number of random objects : this quantity is proportional to the observed-quasar density corrected for completeness. The black dotted lines on Figure 6 show that this ratio varies with all quantities, except star density. This means that we do not observe any bias in the quasar target selection due to blending effects. The dependencies are compatible between the NGC and the SGC, and they do not depend on redshift.

We fit a linear function to the dependency with the depth. We weight each quasar with the inverse of the fitted function for the value of the depth in the considered pixel of the map, and recompute the $n_{\text{QSO}}/n_{\text{random}}$ ratio. The blue lines in Figure 6 show that the dependencies of this ratio with airmass, seeing, sky-flux and depth vanish, and that the dependency with Galactic extinction is reduced, but still significant. The same procedure is applied to the observed-quasar density already corrected for depth to correct for this remaining dependency with Galactic extinction. The final systematic weights for target selection inhomogeneity are obtained by multiplying the depth and Galactic-extinction weights.

4.3 Effect of weightings on $\xi(r)$

Figure 7 shows $r \cdot \xi(r)$ without any weights, and with the successive addition of collision weights, unidentification weights, depth weights and depth plus Galactic-extinction weights. We quantify the effect of the corrections by computing the cross- χ^2 between $\xi_{\text{N}}(r)$ and $\xi_{\text{S}}(r)$, the correlation functions measured in the NGC and the SGC :

$$\chi_{\text{NS}}^2 = \sum_{ij} (\xi_{\text{N}}(r_i) - \xi_{\text{S}}(r_i)) C_{ij}^{-1} (\xi_{\text{N}}(r_j) - \xi_{\text{S}}(r_j)), \quad (4.2)$$

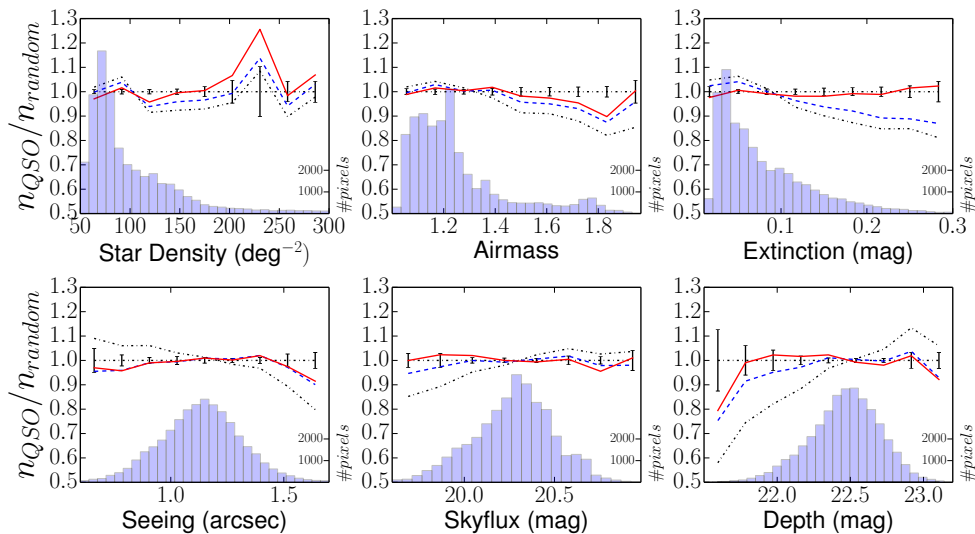


Figure 6. The $n_{\text{QSO}}/n_{\text{randoms}}$ ratio versus star density, airmass, Galactic extinction, seeing, sky-flux and depth, for the i -band before any correction (black dotted lines), after correction by the depth (blue dotted lines), and after correction by the depth and the extinction (red full lines). For the sake of clarity, the error bars, which are similar before and after weighting, are only displayed once on the $n_{\text{QSO}}/n_{\text{randoms}} = 1$ line. The histograms display the distribution of pixels for the healpix maps.

Weighting scheme	χ_{NS}^2 (24 d.o.f.)
No weights	161
Collision	154
Collision + Unidentification	128
Collision + Unidentification + Depth	58
Collision + Unidentification + Depth + Galactic extinction	47

Table 1. Values of χ_{NS}^2 (see Eq. 4.2) for different weighting schemes.

where C is the sum of C_N et C_S , the covariance matrices of $\xi_N(r)$ and $\xi_S(r)$. The resulting values are shown in Table 1. The main effect clearly arises from weighting with the depth, which strongly reduces the value of χ_{NS}^2 . The correction for fiber collisions has only a limited impact on larger scales, and is not susceptible to bias the measure of b_Q . In the following, we will always apply the full weighting scheme to our data sample.

5 Measurement of the quasar bias

In order to measure the quasar bias, b_Q , we fit the measured $\xi(r)$ with a flat Λ CDM model, using the same cosmological parameters used for the BOSS twelfth Data Release (namely $h = 0.676$, $\Omega_m = 0.31$, $\Omega_b h^2 = 0.0220$, $n_s = 0.9619$). Using these parameters, CAMB [100] and HALOFIT [101] provide a non-linear matter power spectrum $P_{\text{mat}}(k)$. We account for linear redshift-space-distortions using the Kaiser formula [102]:

$$P_Q(k, \mu) = b_Q^2 (1 + \beta \mu_k^2)^2 P_{\text{mat}}(k), \quad (5.1)$$

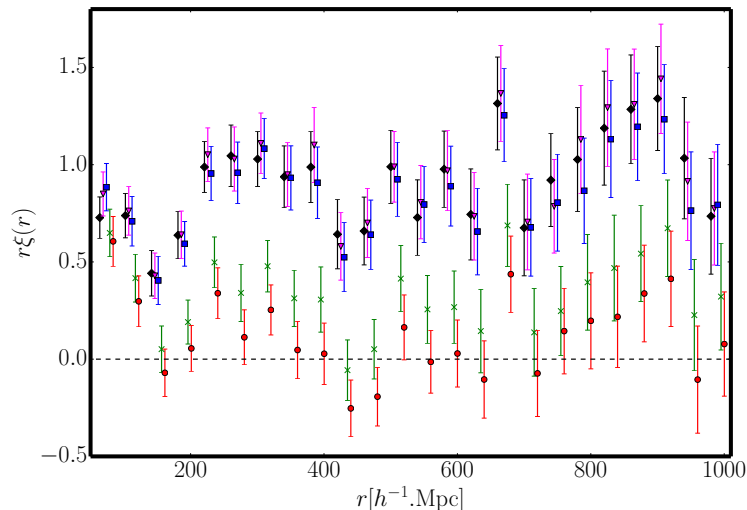


Figure 7. Effects of the different weightings on the quasar correlation function. The black lozenges correspond to $\xi(r)$ without any weighting, the magenta triangles to $\xi(r)$ with the collision weights. The blue squares are obtained with the combination of the collision and unidentification weights, the green crosses are obtained with the addition of the depth weights and the red circles are obtained with the addition of the depth and Galactic-extinction weights.

where μ_k is the cosine of the angle between k and the line of sight, $\beta = f/b_Q$, and $f \simeq \Omega_m^{0.55}(z)$ is the growth rate of structures. The last step consists in converting $P_Q(k)$ into $\xi_Q(r)$ using a Fast Fourier Transform (FFT).

All fits of b_Q are performed using the MINUIT libraries [103] over the range $10 < r < 85 h^{-1}\text{Mpc}$. The fit, shown on Figure 8, exhibits a fair agreement with the ΛCDM model ($\chi^2 = 4.0$ for 7 d.o.f.). For the full eBOSS survey, we measure $b_Q = 2.45 \pm 0.05$, for $\bar{z} = 1.55$. This result is in agreement with the results obtained by Croom et al. [41] using the 2dF QSO Redshift Survey : their empirical parametrization yields a value $b_Q(z = 1.55) = 2.41$. Croom et al. [41] give the error on the two parameters of their fit but not the correlation. If we neglect the correlation, the error on $b_Q(z = 1.55)$ is 0.30. In any case our measurement is compatible with their parametrization. If we fit their data, we confirm their values of a and b , and find a correlation coefficient $\rho_{a,b} = -0.90$. Taking into account this anticorrelation, yields a much lower error on $b_Q(z = 1.55)$ of 0.10. In any case our measurement is compatible with their parametrization.

These results are also compatible with the measurement obtained with the SDSS II quasar sample. The right panel of Figure 8 shows that the ratio $\xi_{QSO}/\xi_{mat} = b_Q^2(1 + \frac{2}{3}\beta + \frac{1}{5}\beta^2)$, where ξ_{mat} is the matter correlation function, remains nearly constant with r . This means that our measurement of b_Q is not sensitive to the range of the fit.

We cut our sample in 4 redshift slices, and measure b_Q in each subsample : the results are displayed on Figure 9, alongside results from the BOSS quasar sample. The numerical values are presented in Table 2. We combine the measurements of b_Q from the eBOSS and BOSS samples, and fit $b_Q(z)$. In order to avoid a large anti-correlation between the fit parameters obtained with Croom parametrization, we use an equivalent parametrization defined such as to yield non correlated parameters :

$$b_Q(z) = \alpha[(1+z)^2 - 6.565] + \beta \quad (5.2)$$

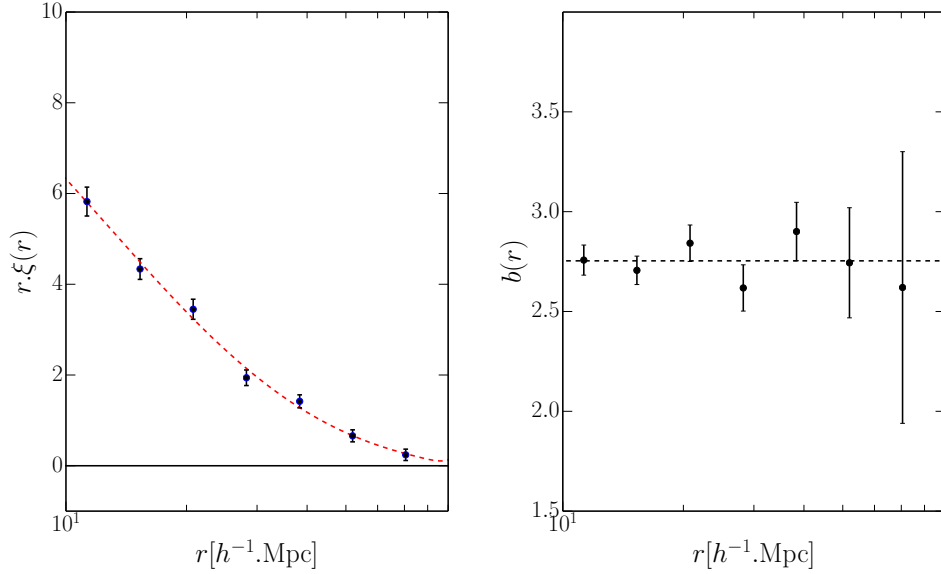


Figure 8. *Left* : $\xi(r)$ for the eBOSS survey (black dots). The red dashed curve is a Λ CDM fit to the data. *Right* : measured quasar effective bias ($\xi_{QSO}/\xi_{mat,CAMB}$) as a function of the separation r . The bias is compatible with a constant, even on larger scales due to systematic weighting.

z_{min}	z_{max}	z_{eff}	N_{QSO}	b_Q	χ^2 (7 d.o.f.)
0.9	1.2	1.06	13,594	1.75 ± 0.08	9.9
1.2	1.5	1.35	17,696	2.06 ± 0.08	1.7
1.5	1.8	1.65	17,907	2.57 ± 0.09	2.1
1.8	2.2	1.99	19,575	3.03 ± 0.11	8.5
0.9	2.2	1.55	68,772	2.43 ± 0.05	4.5

Table 2. Fit of bias over $10 < r < 85 h^{-1}\text{Mpc}$ in various redshift bins.

with

$$\alpha = 0.278 \pm 0.018, \quad \beta = 2.393 \pm 0.042, \quad \rho_{\alpha,\beta} = 0, \quad (5.3)$$

where $\rho_{\alpha,\beta}$ is the correlation coefficient between the parameters α and β . This is equivalent to $a = 0.278 \pm 0.018$, $b = 0.57 \pm 0.13$ and $\rho_{a,b} = -0.94$, consistent with Croom et al.

The right panel of Figure 9 displays the ratio of the quasar bias measured by the 2dF and the SDSS-II surveys to the value of our fitted function. Our results appear again to be compatible with former analyses of quasar clustering. We also stress that, with only one fifth of its final statistic, the eBOSS quasar sample already provides the most accurate measurement of the quasar bias in the redshift range $0.9 < z < 2.2$.

6 The halo mass and the duty cycle of eBOSS quasars

We now discuss possible implications of our measurements of the clustering of $\sim 70,000$ eBOSS quasars for the host dark matter haloes of quasars at $1 \lesssim z \lesssim 2$. We quantify the activity of eBOSS

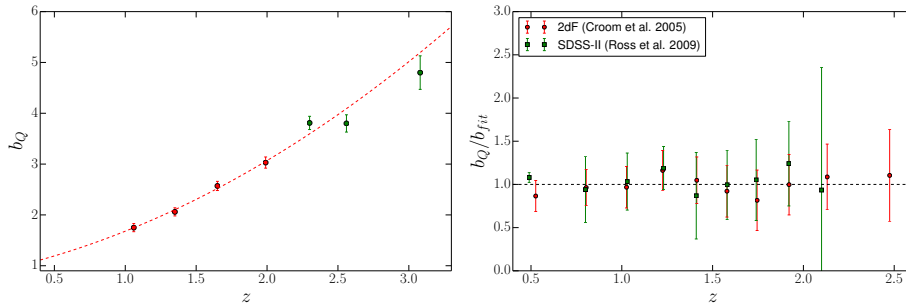


Figure 9. *Left* : measured quasar bias as a function of redshift. The red dots correspond to this analysis (eBOSS data) and the green dots correspond to the bias measured with the BOSS sample, in the range $2.2 < z < 3.5$ [69]. The red dotted line is the fit $b_Q(z) = a(1+z)^2 + b$. *Right* : ratio of quasar bias measured by previous surveys to the value of the function fitted on the results of the eBOSS and BOSS samples. The red dots correspond to the 2dF sample, the blue squares to the SDSS-II quasar sample.

quasars by calculating their duty cycle, through which the halo mass of a population of quasars can be linked to their luminosity.

6.1 Characteristic Halo Mass

Quasars are biased tracers of underlying dark matter [e.g 104] and the fact that more massive haloes have higher clustering bias [105, 106], has been used as the basis for constraining the mass of the dark matter haloes that host quasars [e.g. 49, 104, 107–109]. Here, we follow a similar approach to Eftekharzadeh et al. [49], who constrained the dark matter halo mass and duty cycle of $\sim 75,000$ quasars at $z \sim 2.5$ in the final release of the BOSS survey.

We adopt parameters such as to get a $\Delta = 200$ matter overdensity in the formalism of Tinker et al. [106] in order to calculate the minimum halo mass, $M_{h,\min}$, and the characteristic halo mass, \bar{M}_h , of our quasars. We apply this approach to quasars in our main sample, and in each of our four redshift subsamples (detailed in Table 3). In this formalism, \bar{M}_h is the characteristic halo mass that corresponds to our measured clustering bias, i.e. $b(\bar{M}_h) = b_Q$, and $M_{h,\min}$ is the minimum halo mass that bounds the range of haloes that correspond to the observed clustering bias, i.e. $b(M > M_{h,\min}) = b_Q$, with

$$b(M > M_{h,\min}) \equiv \frac{\int_{M_{h,\min}}^{\infty} \frac{dn}{dM} b(M) dM}{\int_{M_{h,\min}}^{\infty} \frac{dn}{dM} dM}, \quad (6.1)$$

where the halo masses above $M_{h,\min}$ are weighted by the halo abundance dn/dM in the halo mass function as determined by Tinker et al. [110].

The assumption of a lower limit $M_{h,\min}$ in Eqn. 6.1, suggests that haloes with $M < M_{h,\min}$ can only host quasars that are less luminous than the least luminous quasar in our sample. This interpretation can be tested for consistency by checking whether quasar clustering is luminosity-dependent. For example, Eftekharzadeh et al. [49] found that the assumption of a scatter-less monotonic relation between halo mass and quasar luminosity failed to describe the observed lack of luminosity dependence for the clustering of BOSS quasars at $z \sim 2.4$. How quasar clustering varies with luminosity appears to be a subtle effect. Categorically detecting whether different luminosity quasars are hosted by different mass haloes will therefore require very precise measurements of quasar clustering. Con-

straining any luminosity dependence to quasar clustering is a topic where eBOSS could make gains, given its expected unprecedentedly large sample of homogeneously selected quasars.

Prior to eBOSS, the most extensive wide-area spectroscopic quasar surveys at $z \sim 1.5$ that were used for clustering analyses, were the 2dFQSO redshift survey [111, 112, 2QZ;] and the SDSS-DR5 quasar survey [113, 114, DRQ5;]. Restricting to uniformly selected quasars over the redshift range $0.9 < z < 2.2$, these surveys provided catalogs of $\sim 20,000$ – $25,000$ quasars with which to conduct clustering analyses. Projecting from SEQUELS, eBOSS is expected to spectroscopically confirm ~ 70 quasars per deg^2 down to a limiting magnitude of $g < 22$ over $\sim 7,500 \text{ deg}^2$, for a total sample of more than 500,000 uniformly selected quasars in the redshift range $0.9 < z < 2.2$ [83]. The average magnitude of eBOSS quasars is ~ 2.5 times fainter than that of previous SDSS clustering samples, while covering a similar redshift range. Essentially, therefore, eBOSS will extend quasar clustering measurements by about a factor of 10 in luminosity. This unprecedented expansion of the dynamical range and number density of quasar samples will allow eBOSS to provide the highest statistical power yet to disentangle the luminosity and redshift dependences of quasar clustering.

Figure 10 shows $M_{h,\min}$ and \bar{M}_h for our full (NGC+SGC) sample of 68,772 quasars at $z \sim 1.5$, as well as for our four redshift subsamples at $z = 1.06, 1.35, 1.65,$ and 1.99 . In addition, the 4th and 5th columns of Table 4 list the \bar{M}_h and $M_{h,\min}$ we derive for our four redshift subsamples as well as for our main sample. The errors on \bar{M}_h and $M_{h,\min}$ are calculated from the confidence intervals for the quasar biases that we derive from our clustering measurements. These confidence intervals are projected through Eqn. 6.1 at the mean redshift of each sample, using the Tinker et al. [110] halo mass function and the appropriate values of $M_{h,\min}$, in order to derive a corresponding confidence interval in halo mass.

To illustrate how $M_{h,\min}$ and \bar{M}_h change over the redshift range that is covered by both BOSS ($z > 2.2$) and eBOSS ($z < 2.2$), Figure 10 displays the measurements made by Eftekharzadeh et al. [49] for BOSS quasars using the same formalism that we use here for eBOSS quasars. Figure 10 also includes the same quantities estimated using the quasar clustering measurements from Shen et al. [45] at $z \sim 3.1$ and $z \sim 4.0$ and Font-Ribera et al. [115] at $z \sim 2.4$. Note that the agreement between Font-Ribera et al. [115] and Eftekharzadeh et al. [49] is not particularly surprising, as both measurements are made using BOSS quasars. However, the reason for the extreme differences in halo mass measured by Shen et al. [45], as compared to lower-redshift studies, remains debatable. Shen et al. [45] studied the clustering of a sample of ~ 4000 highly luminous quasars with a density of $\sim 1 \text{ deg}^{-2}$ and measured quasar biases approaching $b_Q \sim 16$ at $z > 4$. It is possible that there is a sharp change in the host halo mass of quasars that lie beyond the luminosity and redshift range of BOSS — models in which quasars are triggered by major mergers of gas-rich galaxies [e.g. 116] do allow for evolutionary scenarios in which the clustering of luminous quasars simply tracks the growth of the most massive haloes at $z > 3$. Indeed, the duty cycle of $f_{\text{duty}} \sim 1$ measured by Shen et al. [45] for quasars at $z > 3$ implies that *all* rare supermassive haloes ($> 10^{13} M_\odot$) host active black holes.

Previous authors [e.g. 112] found convincing evidence that the bias of $z < 2.5$ quasars, at magnitudes of about $g < 21$, increases with redshift from $z \sim 0.5$ to $z \sim 2.5$. This implies that the mass of the haloes hosting quasars remains fairly constant at $z < 2.5$, because a higher bias can offset the fact that the characteristic mass of the average halo must dwindle at higher redshift (as structure has had less time to grow). By extension, if the bias of quasars were to remain constant at higher and higher redshift, this would imply that the characteristic mass of the haloes hosting quasars was decreasing with redshift. Essentially this dwindling host halo mass was what was found by Eftekharzadeh et al. [49] for BOSS quasars at $z > 2.5$, as is shown in Figure 10. Contrary to the flat $b_Q(z)$, or dwindling host halo mass, measured for BOSS quasars at $z > 2.5$, the biases we measure for eBOSS quasars increase with redshift, implying that the characteristic host halo mass of eBOSS

quasars is roughly constant (again as shown in Figure 10). This is in excellent agreement with the results of Croom et al. [112], who found a non-evolving halo mass of $M = (3.0 \pm 1.6) \times 10^{12} h^{-1} M_{\odot}$ over $0.5 < z < 2.5$ for a smaller sample of quasars that were slightly more luminous than those in our sample.

6.2 Duty Cycle

The length of duration of the quasar phase (the so-called ‘‘duty cycle’’) has been defined in multiple slightly different ways in the literature. Here, we take the definition of the duty cycle as the ratio of the number density of haloes that host black holes that are ‘‘on’’ (and thus observed as luminous quasars) to the full number of haloes that could host quasars within the luminosity range of our sample. As in Eftekharzadeh et al. [49], we compare the cumulative luminosity function of quasars over a range of luminosities to the cumulative space density of haloes over the corresponding range of host halo masses [e.g. 104, 108]

$$f_{\text{duty}} = \frac{\int_{L_{\text{min}}}^{L_{\text{max}}} \Phi(L) dL}{\int_{M_{h,\text{min}}}^{\infty} \frac{dn}{dM} dM}, \quad (6.2)$$

where the value of $M_{h,\text{min}}$ is set by the measured quasar bias (as in Eqn. 6.1), dn/dM is, again, taken from Tinker et al. [110], and $\Phi(L)$ is the quasar luminosity function. Note that we integrate our halo masses over the entire mass range from $M_{h,\text{min}}$ to infinity. Effectively, this reflects the extremely weak relationship between quasar clustering and quasar luminosity, by allowing the quasars in our samples to be hosted by a limitless range of halo masses above $M_{h,\text{min}}$. We adopt a recent quasar luminosity function from Palanque-Delabrouille et al. [84] that was derived using quasars in our redshift and luminosity ranges of interest. We use this luminosity function to calculate the space density of quasars in our samples (see the 3rd column in Table 4). Quasars targeted as part of eBOSS do not all receive a fiber for follow-up spectroscopy. Further, eBOSS is not complete to *all* quasars in the Universe. Hence, the observed number density of quasars listed in Table 3 should be lower than the expected total space density of $0.9 < z < 2.2$ quasars at the flux limit of eBOSS, even if the Palanque-Delabrouille et al. [84] luminosity function is perfectly accurate.

We display our calculated f_{duty} values as a function of redshift in Figure 11 and list the corresponding measurements in Table 4. We estimate errors on f_{duty} by drawing sample values of the quasar bias from a Gaussian corresponding to the 68% confidence interval around our measured $\pm 1\sigma$ errors on b_Q . We then calculate f_{duty} for each sampled b_Q using Eqn. 6.1 and Eqn. 6.2, and hence derive the implied $\pm 1\sigma$ errors on f_{duty} . Figure 11 compares our results to the similarly calculated $f_{\text{duty}}(z)$ of BOSS quasars at $z > 2.2$ from Eftekharzadeh et al. [49].

Under the assumption that there is effectively no link between the luminosity and clustering of quasars (i.e. the assumption that we used to derive f_{duty}), we can ignore the different luminosity ranges probed by BOSS and eBOSS and directly compare the host halo masses and duty cycles of BOSS and eBOSS quasars. The almost flat $\bar{M}_h(z)$ up until $z \sim 1.8$ depicted in Figure 10, implies that quasars reside in haloes of similar mass at $z \lesssim 2$. Above $z \sim 2$, the characteristic mass of the haloes that host quasars appears to plummet, by almost a dex by $z \sim 3$. Further, as listed in Table 4, the measured duty cycle for eBOSS quasars at $\bar{z} \sim 1.5$ is more than four times longer than for BOSS quasars at $\bar{z} \sim 2.5$. It has long been known that the quasar population peaks in space density around redshift 2–3 [e.g. 117]. We can interpret this peak as a physical manifestation

of a combination of the quasar duty cycle and the characteristic masses of quasar-hosting haloes. As more massive haloes are rarer, $z \sim 2$ –3 is a sweet-spot where duty cycles are large compared to host halo rarity. Below $z \sim 2$ quasar-hosting haloes are equally as rare as they are at $z \sim 2$ (because

Δz	ΔM_i	N_{qso}	n ($10^{-6} h^{-1} \text{Mpc}^{-3}$)
$0.9 \leq z < 1.2$	$-22.05 \leq M_i \leq -26.77$	13594	13.94 ± 0.27
$1.2 \leq z < 1.5$	$-22.62 \leq M_i \leq -27.33$	17696	15.20 ± 0.26
$1.5 \leq z < 1.8$	$-22.97 \leq M_i \leq -27.81$	17907	13.98 ± 0.27
$1.8 \leq z < 2.2$	$-23.49 \leq M_i \leq -28.22$	19575	10.87 ± 0.30
$0.9 \leq z \leq 2.2$	$-22.82 \leq M_i \leq -27.67$	68772	13.17 ± 0.28

Table 3. The redshift limits, absolute i -magnitude range, total number of quasars (NGC+SGC) and space density in comoving coordinates for quasars in our main sample (final row) and redshift subsamples.

the characteristic halo mass is unchanging) but the increasingly small duty cycle at lower redshifts implies that fewer of these haloes host active quasars. In contrast, at $z \sim 2\text{--}3$, the characteristic mass of quasar-hosting haloes drops, which implies that quasar-hosting haloes are more common. This, however, is offset somewhat by a rapid reduction in the duty cycle, which implies that at higher redshifts in the range $z \sim 2\text{--}3$ fewer and fewer quasars are “on” in these increasingly more numerous haloes.

On the other hand, our assumption that there is absolutely no correlation between quasar luminosity and host halo mass may break down under further scrutiny. More sophisticated models that add scatter to the halo mass-luminosity relation [e.g. 118] would then be needed to fully understand the interplay between quasars and large-scale structure. The characteristic mass of the haloes that host quasars is an average across the halo mass function (dn/dM), so the fact that the characteristic mass stays relatively constant between $z \sim 2$ and $z \sim 1$ could simply mean that the most massive haloes dominate this average. A plausible scenario might be that less luminous quasars inhabit a wide range of halo masses but more luminous quasars only reside in the most massive haloes. At $z \sim 1$, where we sample far down the quasar luminosity function, we might then expect to see a wide range of halo masses, but the clustering signal would still be dominated by the most massive haloes. At $z \sim 2$, where our magnitude-limited sample would shift to more luminous quasars, we would increasingly sample just higher-mass haloes. In either case, at $z \sim 1$ or at $z \sim 2$ our clustering signal would only reflect the clustering of high mass haloes. It is straightforward to interpret our measurements under this alternative scenario. For example, Table 4 shows that quasars in our first redshift subsample at $0.9 < z < 1.2$ are the least luminous population, on average, among our four redshift subsamples, and that there are also fewer of them. These $0.9 < z < 1.2$ quasars have an $M_{h,\text{min}}$ that is somewhat smaller than the $2\text{--}3\times$ more luminous population at $1.5 < z < 1.8$, but have an \bar{M}_h that is consistent. This could be interpreted to be indicative of the less-luminous-than average $0.9 < z < 1.2$ quasars occupying the widest range of halo masses in eBOSS but, also being less numerous, still having a clustering signal that is dominated by the most massive haloes.

Our sample of quasars is of insufficient size to detect any luminosity dependence to quasar clustering. But, as was mentioned earlier in this section, a detailed study of the luminosity dependence of quasar clustering using the final eBOSS sample of $\sim 500,000$ quasars remains an important and highly anticipated objective of the eBOSS survey. In addition, the quasars sampled by eBOSS overlap the Luminous Red Galaxy and Emission Line Galaxy populations sampled by eBOSS around $0.7 \lesssim z \lesssim 1.0$. This will provide a chance to cross correlate quasars with more-numerous galaxies [as in, e.g., 119, 120] to try to study the luminosity dependence of quasar clustering in narrow redshift bins near $z \sim 0.8$.

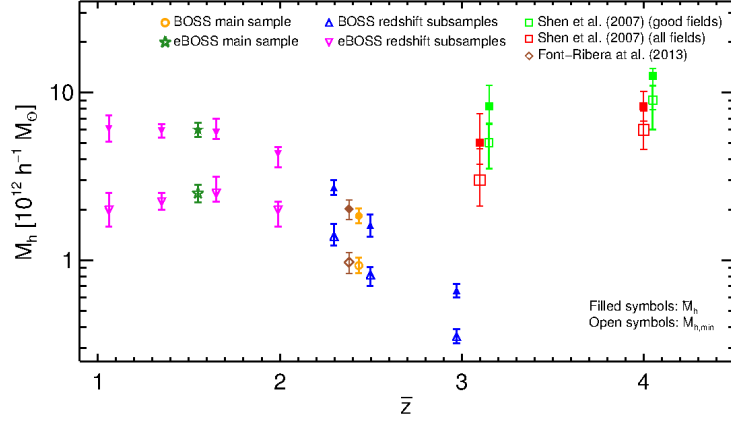


Figure 10. The evolution of the minimum and characteristic halo mass (see also Eqn. 6.1 and Table 4) for our full sample (green stars) and four redshift subsamples (pink inverted triangles). Other points indicate the results for BOSS from Eftekharzadeh et al. [49] for their main sample (orange circle) and three redshift subsamples (blue triangles), from Shen et al. [45, the "good fields" points have been offset slightly for visual clarity], and from Font-Ribera et al. [115]. Results from previous works are based on their reported values of quasar bias, recalibrated to our chosen cosmology.

Δz	ΔL (10^{46} erg s $^{-1}$)	$\Phi(L_{\min} < L < L_{\max})$ ($10^{-6} h^{-1} \text{Mpc})^{-3}$	$M_{h,\min}$ ($10^{12} h^{-1} M_{\odot}$)	\bar{M}_h ($10^{12} h^{-1} M_{\odot}$)	f_{duty}
$0.9 \leq z < 1.2$	$0.04 \leq L \leq 2.96$	$16.96^{+1.54}_{-1.78}$	$1.99^{+0.52}_{-0.41}$	$6.10^{+1.20}_{-1.00}$	0.0091 ± 0.0027
$1.2 \leq z < 1.5$	$0.06 \leq L \leq 4.94$	$23.69^{+2.46}_{-2.19}$	$2.24^{+0.27}_{-0.24}$	$5.91^{+0.56}_{-0.51}$	0.0183 ± 0.0028
$1.5 \leq z < 1.8$	$0.09 \leq L \leq 7.68$	$29.37^{+2.91}_{-2.99}$	$2.51^{+0.65}_{-0.27}$	$5.80^{+1.20}_{-0.51}$	0.0355 ± 0.0133
$1.8 \leq z \leq 2.2$	$0.14 \leq L \leq 11.23$	$32.89^{+3.10}_{-3.56}$	$1.99^{+0.24}_{-0.41}$	$4.33^{+0.42}_{-0.74}$	0.0422 ± 0.0077
$0.9 \leq z \leq 2.2$	$0.04 \leq L \leq 11.23$	$26.82^{+2.11}_{-2.42}$	$2.51^{+0.31}_{-0.27}$	$6.01^{+0.58}_{-0.58}$	0.0292 ± 0.0048

Table 4. The first two columns display the redshift limits and luminosity range for our main sample (final row) and redshift subsamples. The 3rd column lists the space density of quasars in the given redshift and luminosity ranges, calculated using the combination of the Pure Luminosity Evolution (PLE) and the Luminosity and Density Evolution (LEDE) models for the luminosity function (PLE+LEDE) from Palanque-Delabrouille et al. [84]. The 4th and 5th columns display the minimum and the characteristic halo mass calculated at the average redshift of the sample (see Eqn. 6.1). The 6th column lists the duty cycle, which is derived from $M_{h,\min}$ and Φ (see Eqn. 6.2). f_{duty} is expressed as a fraction of the Hubble time ($9.785 h^{-1}$ Gyr in our adopted cosmology).

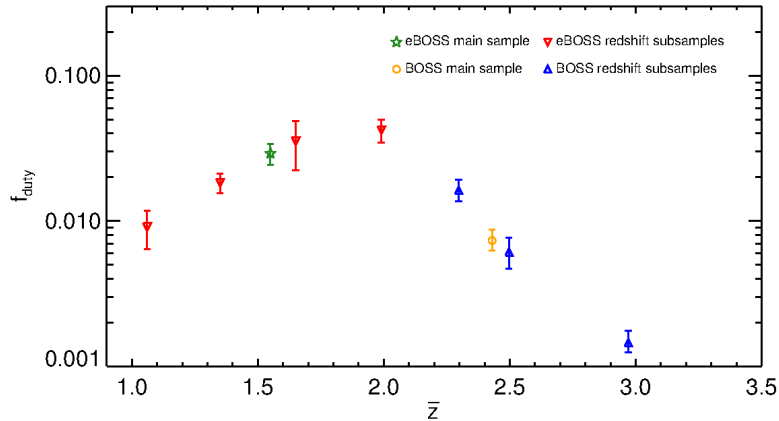


Figure 11. The evolution of the duty cycle for our main sample (green star) and four redshift subsamples (red inverted triangles) calculated using Eqn. 6.2. See Table 4 for the f_{duty} values and Table 3 for a summary of each sample’s physical properties. Triangles depict values of f_{duty} for BOSS quasars from Eftekharzadeh et al. [49] for their main sample (orange circle) and their three redshift subsamples (blue triangles).

7 Conclusion

The first year of observation of the eBOSS survey provides 68,772 homogeneously selected quasars in the redshift range $0.9 < z < 2.2$, which represents the largest quasar sample ever obtained in this redshift range. We use this quasar sample to measure the quasar correlation function $\xi(r)$. We investigate various sources of systematic effects that might impact the measurement of $\xi(r)$, and find that the main contribution arises from inhomogeneities in the quasar target selection. We provide a weighting scheme that mitigates the important systematic effects, and we show that the resulting correlation function is much closer to zero on large scales

The measured correlation function is in agreement with a linear Λ -CDM model in the range $10 < r < 85 h^{-1}\text{Mpc}$. We measure the quasar bias of our sample to be $b_Q = 2.45 \pm 0.05$, at $\bar{z} = 1.55$. Splitting our sample into four redshift slices provides the evolution of b_Q with redshift, and confirms that b_Q increases with z in the studied redshift range. These results are compatible with previous findings by the 2dF and SDSS-II surveys. It is also remarkable that, with only one fifth of the final sample, the eBOSS survey already provides the most accurate measurement of $b_Q(z)$ in the range $0.9 < z < 2.2$.

Adopting Tinker et al. [106]’s formalism for the the dark matter distribution and halo mass function, we calculate the minimum halo mass, $M_{h,\text{min}}$, and the characteristic halo mass, \bar{M}_h , of our quasar sample. We use a recent luminosity function that was derived using quasars in our redshift and luminosity ranges of interest [84] to measure the duty cycle of eBOSS quasars at $z \sim 1.5$ and for subsamples of these quasars in four slices of redshift over $0.9 < z < 2.2$ to investigate the redshift evolution of $M_{h,\text{min}}$, \bar{M}_h , and f_{duty} . We conduct our $M_{h,\text{min}}$, \bar{M}_h , and f_{duty} calculations under the assumption that there is weak to no connection between quasar clustering and quasar luminosity. This assumption allowed us to compare the same calculations for BOSS quasars at $z > 2.2$ to our measurements for much fainter quasars at $z < 2.2$.

We find that the characteristic mass of haloes hosting quasars remains relatively constant at $z < 2.2$. This finding is in agreement with the non-evolving halo mass of quasars over $0.5 < z < 2.2$

found by Croom et al. [112]. Our result is also in accord with the dwindling halo mass found for BOSS quasars at $z > 2.2$ by Eftekharzadeh et al. [49] as the structures have more time to grow at higher redshifts than at $z < 2$ (see Fig. 10). We find the duty cycle of eBOSS quasars at $\bar{z} \sim 1.5$ to be more than four times longer than that of BOSS quasars at $\bar{z} \sim 2.5$. Combining the duty cycles of BOSS and eBOSS quasars in Fig. 11, we interpret the observed peak at the quasar duty cycle around $z \sim 2$ as a physical manifestation of having fewer quasars that are “on” at $z \sim 2-3$. The average luminosity of eBOSS quasars at $0.9 < z < 1.2$ in our sample is 2-3 times less than quasars at $1.5 < z < 1.8$ and they appear to occupy a wider range of halo masses with smaller $M_{h,\min}$ compared to quasars at $1.5 < z < 1.8$ (see Table 4). Nevertheless, the clustering signal for both sets of quasars is dominated by the rare most massive halos in their occupied range of halo masses. The size of our current sample of quasars in the first year of eBOSS is insufficient to detect any luminosity dependence to quasar clustering. Whether quasar clustering is luminosity-dependent will be further investigated with the final sample of $\sim 500,000$ eBOSS quasars.

Acknowledgements

Funding for the Sloan Digital Sky Survey IV has been provided by the Alfred P. Sloan Foundation, the U.S. Department of Energy Office of Science, and the Participating Institutions. SDSS acknowledges support and resources from the Center for High-Performance Computing at the University of Utah. The SDSS web site is www.sdss.org.

SDSS is managed by the Astrophysical Research Consortium for the Participating Institutions of the SDSS Collaboration including the Brazilian Participation Group, the Carnegie Institution for Science, Carnegie Mellon University, the Chilean Participation Group, the French Participation Group, Harvard-Smithsonian Center for Astrophysics, Instituto de Astrofísica de Canarias, The Johns Hopkins University, Kavli Institute for the Physics and Mathematics of the Universe (IPMU) / University of Tokyo, Lawrence Berkeley National Laboratory, Leibniz Institut für Astrophysik Potsdam (AIP), Max-Planck-Institut für Astronomie (MPIA Heidelberg), Max-Planck-Institut für Astrophysik (MPA Garching), Max-Planck-Institut für Extraterrestrische Physik (MPE), National Astronomical Observatories of China, New Mexico State University, New York University, University of Notre Dame, Observatório Nacional / MCTI, The Ohio State University, Pennsylvania State University, Shanghai Astronomical Observatory, United Kingdom Participation Group, Universidad Nacional Autónoma de México, University of Arizona, University of Colorado Boulder, University of Oxford, University of Portsmouth, University of Utah, University of Virginia, University of Washington, University of Wisconsin, Vanderbilt University, and Yale University.

References

- [1] Smoot, G. F., C. L. Bennett, A. Kogut, et al. Structure in the COBE differential microwave radiometer first-year maps. *Astrophys. J. Lett.*, 396:L1–L5, 1992.
- [2] Bennett, C. L., A. J. Banday, K. M. Gorski, et al. Four-Year COBE DMR Cosmic Microwave Background Observations: Maps and Basic Results. *Astrophys. J. Lett.*, 464:L1, 1996. [astro-ph/9601067](https://arxiv.org/abs/astro-ph/9601067).
- [3] Bennett, C. L., M. Halpern, G. Hinshaw, et al. First-Year Wilkinson Microwave Anisotropy Probe (WMAP) Observations: Preliminary Maps and Basic Results. *Astrophys. J. Suppl.*, 148:1–27, 2003. [astro-ph/0302207](https://arxiv.org/abs/astro-ph/0302207).
- [4] Komatsu, E., J. Dunkley, M. R. Nolta, et al. Five-Year Wilkinson Microwave Anisotropy Probe Observations: Cosmological Interpretation. *Astrophys. J. Suppl.*, 180:330–376, 2009. [arXiv:0803.0547](https://arxiv.org/abs/0803.0547).

- [5] Planck Collaboration, P. A. R. Ade, N. Aghanim, et al. Planck 2013 results. XVI. Cosmological parameters. *Astron. and Astrophys.*, 571:A16, 2014. [arXiv:1303.5076](#).
- [6] Planck Collaboration, P. A. R. Ade, N. Aghanim, et al. Planck 2015 results. XIII. Cosmological parameters. *ArXiv e-prints*, 2015. [arXiv:1502.01589](#).
- [7] Chevallier, M. and D. Polarski. Accelerating Universes with Scaling Dark Matter. *International Journal of Modern Physics D*, 10:213–223, 2001. [gr-qc/0009008](#).
- [8] Linder, E. V. Cosmic growth history and expansion history. *Phys. Rev. D*, 72:043529, 2005. [astro-ph/0507263](#).
- [9] Weinberg, D. H., M. J. Mortonson, D. J. Eisenstein, et al. Observational probes of cosmic acceleration. *Phys. Rep.*, 530:87–255, 2013. [arXiv:1201.2434](#).
- [10] Drinkwater, M. J., R. J. Jurek, C. Blake, et al. The WiggleZ Dark Energy Survey: survey design and first data release. *Mon. Not. Roy. Astron. Soc.*, 401:1429–1452, 2010. [arXiv:0911.4246](#).
- [11] Adams, J. J., G. A. Blanc, G. J. Hill, et al. The HETDEX Pilot Survey. I. Survey Design, Performance, and Catalog of Emission-line Galaxies. *Astrophys. J. Suppl.*, 192:5, 2011. [arXiv:1011.0426](#).
- [12] Dawson, K. S., D. J. Schlegel, C. P. Ahn, et al. The Baryon Oscillation Spectroscopic Survey of SDSS-III. *Astronom. J.*, 145:10, 2013. [arXiv:1208.0022](#).
- [13] Levi, M., C. Bebek, T. Beers, et al. The DESI Experiment, a whitepaper for Snowmass 2013. *ArXiv e-prints*, 2013. [arXiv:astro-ph.CO/1308.0847](#).
- [14] Dawson, K. S., J.-P. Kneib, W. J. Percival, et al. The SDSS-IV Extended Baryon Oscillation Spectroscopic Survey: Overview and Early Data. *Astronom. J.*, 151:44, 2016. [arXiv:1508.04473](#).
- [15] Huchra, J., M. Davis, D. Latham, et al. A survey of galaxy redshifts. IV - The data. *Astrophys. J. Suppl.*, 52:89–119, 1983.
- [16] Shectman, S. A., S. D. Landy, A. Oemler, et al. The Las Campanas Redshift Survey. *Astrophys. J.*, 470:172, 1996. [astro-ph/9604167](#).
- [17] Saunders, W., W. J. Sutherland, S. J. Maddox, et al. The PSCz catalogue. *Mon. Not. Roy. Astron. Soc.*, 317:55–63, 2000. [astro-ph/0001117](#).
- [18] Colless, M., G. Dalton, S. Maddox, et al. The 2dF Galaxy Redshift Survey: spectra and redshifts. *Mon. Not. Roy. Astron. Soc.*, 328:1039–1063, 2001. [astro-ph/0106498](#).
- [19] Newman, J. A., M. C. Cooper, M. Davis, et al. The DEEP2 Galaxy Redshift Survey: Design, Observations, Data Reduction, and Redshifts. *Astrophys. J. Suppl.*, 208:5, 2013. [arXiv:1203.3192](#).
- [20] York, D. G., J. Adelman, J. E. Anderson, Jr., et al. The Sloan Digital Sky Survey: Technical Summary. *Astronom. J.*, 120:1579–1587, 2000. [astro-ph/0006396](#).
- [21] Strauss, M. A., D. H. Weinberg, R. H. Lupton, et al. Spectroscopic Target Selection in the Sloan Digital Sky Survey: The Main Galaxy Sample. *Astronom. J.*, 124:1810–1824, 2002. [astro-ph/0206225](#).
- [22] Eisenstein, D. J., J. Annis, J. E. Gunn, et al. Spectroscopic Target Selection for the Sloan Digital Sky Survey: The Luminous Red Galaxy Sample. *Astronom. J.*, 122:2267–2280, 2001. [astro-ph/0108153](#).
- [23] Percival, W. J., W. Sutherland, J. A. Peacock, et al. Parameter constraints for flat cosmologies from cosmic microwave background and 2dFGRS power spectra. *Mon. Not. Roy. Astron. Soc.*, 337:1068–1080, 2002. [astro-ph/0206256](#).
- [24] Tegmark, M., M. R. Blanton, M. A. Strauss, et al. The Three-Dimensional Power Spectrum of Galaxies from the Sloan Digital Sky Survey. *Astrophys. J.*, 606:702–740, 2004. [astro-ph/0310725](#).

- [25] Tegmark, M., M. A. Strauss, M. R. Blanton, et al. Cosmological parameters from SDSS and WMAP. *Phys. Rev. D*, 69:103501, 2004. [astro-ph/0310723](#).
- [26] Hogg, D. W., D. J. Eisenstein, M. R. Blanton, et al. Cosmic Homogeneity Demonstrated with Luminous Red Galaxies. *Astrophys. J.*, 624:54–58, 2005. [astro-ph/0411197](#).
- [27] Sánchez, A. G., C. M. Baugh, W. J. Percival, et al. Cosmological parameters from cosmic microwave background measurements and the final 2dF Galaxy Redshift Survey power spectrum. *Mon. Not. Roy. Astron. Soc.*, 366:189–207, 2006. [astro-ph/0507583](#).
- [28] Tegmark, M., D. J. Eisenstein, M. A. Strauss, et al. Cosmological constraints from the SDSS luminous red galaxies. *Phys. Rev. D*, 74:123507, 2006. [astro-ph/0608632](#).
- [29] Cole, S., W. J. Percival, J. A. Peacock, et al. The 2dF Galaxy Redshift Survey: power-spectrum analysis of the final data set and cosmological implications. *Mon. Not. Roy. Astron. Soc.*, 362:505–534, 2005. [astro-ph/0501174](#).
- [30] Eisenstein, D. J., I. Zehavi, D. W. Hogg, et al. Detection of the Baryon Acoustic Peak in the Large-Scale Correlation Function of SDSS Luminous Red Galaxies. *Astrophys. J.*, 633:560–574, 2005. [astro-ph/0501171](#).
- [31] Magorrian, J., S. Tremaine, D. Richstone, et al. The Demography of Massive Dark Objects in Galaxy Centers. *Astronom. J.*, 115:2285–2305, 1998. [astro-ph/9708072](#).
- [32] Richstone, D., E. A. Ajhar, R. Bender, et al. Supermassive black holes and the evolution of galaxies. *Nature*, 395:A14, 1998. [astro-ph/9810378](#).
- [33] Ferrarese, L. and D. Merritt. A Fundamental Relation between Supermassive Black Holes and Their Host Galaxies. *Astrophys. J. Lett.*, 539:L9–L12, 2000. [astro-ph/0006053](#).
- [34] Gebhardt, K., R. Bender, G. Bower, et al. A Relationship between Nuclear Black Hole Mass and Galaxy Velocity Dispersion. *Astrophys. J. Lett.*, 539:L13–L16, 2000. [astro-ph/0006289](#).
- [35] Croom, S. M., R. J. Smith, B. J. Boyle, et al. The 2dF QSO Redshift Survey - XII. The spectroscopic catalogue and luminosity function. *Mon. Not. Roy. Astron. Soc.*, 349:1397–1418, 2004. [astro-ph/0403040](#).
- [36] Richards, G. T., X. Fan, H. J. Newberg, et al. Spectroscopic Target Selection in the Sloan Digital Sky Survey: The Quasar Sample. *Astronom. J.*, 123:2945–2975, 2002. [astro-ph/0202251](#).
- [37] Schneider, D. P., G. T. Richards, P. B. Hall, et al. The Sloan Digital Sky Survey Quasar Catalog. V. Seventh Data Release. *Astronom. J.*, 139:2360, 2010. [arXiv:1004.1167](#).
- [38] Hoyle, F., P. J. Outram, T. Shanks, et al. The 2dF QSO Redshift Survey - VII. Constraining cosmology from redshift-space distortions via $\xi(\sigma, \pi)$. *Mon. Not. Roy. Astron. Soc.*, 332:311–324, 2002. [astro-ph/0107348](#).
- [39] Outram, P. J., F. Hoyle, T. Shanks, et al. The 2dF QSO Redshift Survey - XI. The QSO power spectrum. *Mon. Not. Roy. Astron. Soc.*, 342:483–495, 2003. [astro-ph/0302280](#).
- [40] Outram, P. J., T. Shanks, B. J. Boyle, et al. The 2dF QSO Redshift Survey - XIII. A measurement of Λ from the quasi-stellar object power spectrum, $P^S(k_\perp, k_\parallel)$. *Mon. Not. Roy. Astron. Soc.*, 348:745–752, 2004. [astro-ph/0310873](#).
- [41] Croom, S. M., B. J. Boyle, T. Shanks, et al. The 2dF QSO Redshift Survey - XIV. Structure and evolution from the two-point correlation function. *Mon. Not. Roy. Astron. Soc.*, 356:415–438, 2005. [astro-ph/0409314](#).
- [42] Myers, A. D., R. J. Brunner, R. C. Nichol, et al. Clustering Analyses of 300,000 Photometrically Classified Quasars. I. Luminosity and Redshift Evolution in Quasar Bias. *Astrophys. J.*, 658:85–98, 2007. [astro-ph/0612190](#).

- [43] Myers, A. D., R. J. Brunner, G. T. Richards, et al. Clustering Analyses of 300,000 Photometrically Classified Quasars. II. The Excess on Very Small Scales. *Astrophys. J.*, 658:99–106, 2007. [astro-ph/0612191](#).
- [44] Coil, A. L., J. F. Hennawi, J. A. Newman, et al. The DEEP2 Galaxy Redshift Survey: Clustering of Quasars and Galaxies at $z = 1$. *Astrophys. J.*, 654:115–124, 2007. [astro-ph/0607454](#).
- [45] Shen, Y., M. A. Strauss, M. Oguri, et al. Clustering of High-Redshift ($z \geq 2.9$) Quasars from the Sloan Digital Sky Survey. *Astronom. J.*, 133:2222–2241, 2007. [astro-ph/0702214](#).
- [46] Ross, N. P., Y. Shen, M. A. Strauss, et al. Clustering of Low-redshift ($z \leq 2.2$) Quasars from the Sloan Digital Sky Survey. *Astrophys. J.*, 697:1634–1655, 2009. [arXiv:0903.3230](#).
- [47] Shen, Y., M. A. Strauss, N. P. Ross, et al. Quasar Clustering from SDSS DR5: Dependences on Physical Properties. *Astrophys. J.*, 697:1656–1673, 2009. [arXiv:0810.4144](#).
- [48] White, M., A. D. Myers, N. P. Ross, et al. The clustering of intermediate-redshift quasars as measured by the Baryon Oscillation Spectroscopic Survey. *Mon. Not. Roy. Astron. Soc.*, 424:933–950, 2012. [arXiv:1203.5306](#).
- [49] Eftekharzadeh, S., A. D. Myers, M. White, et al. Clustering of intermediate redshift quasars using the final SDSS III-BOSS sample. *Mon. Not. Roy. Astron. Soc.*, 453:2779–2798, 2015. [arXiv:1507.08380](#).
- [50] Conroy, C. and M. White. A Simple Model for Quasar Demographics. *Astrophys. J.*, 762:70, 2013. [arXiv:1208.3198](#).
- [51] Krumpe, M., T. Miyaji, A. L. Coil, et al. The Spatial Clustering of ROSAT All-Sky Survey Active Galactic Nuclei. III. Expanded Sample and Comparison with Optical Active Galactic Nuclei. *Astrophys. J.*, 746:1, 2012. [arXiv:1110.5648](#).
- [52] Krumpe, M., T. Miyaji, B. Husemann, et al. The Spatial Clustering of ROSAT All-Sky Survey Active Galactic Nuclei. IV. More Massive Black Holes Reside in More Massive Dark Matter Halos. *Astrophys. J.*, 815:21, 2015. [arXiv:1509.01261](#).
- [53] Allevalo, V., A. Finoguenov, and N. Cappelluti. Clustering of γ -Ray-selected 2LAC Fermi Blazars. *Astrophys. J.*, 797:96, 2014. [arXiv:1410.0358](#).
- [54] Allevalo, V., A. Finoguenov, F. Civano, et al. Clustering of Moderate Luminosity X-Ray-selected Type 1 and Type 2 AGNs at $Z \sim 3$. *Astrophys. J.*, 796:4, 2014. [arXiv:1409.7693](#).
- [55] Georgakakis, A., G. Mountrichas, M. Salvato, et al. Large-scale clustering measurements with photometric redshifts: comparing the dark matter haloes of X-ray AGN, star-forming and passive galaxies at $z \approx 1$. *Mon. Not. Roy. Astron. Soc.*, 443:3327–3340, 2014. [arXiv:1407.1863](#).
- [56] Hickox, R. C., J. R. Mullaney, D. M. Alexander, et al. Black Hole Variability and the Star Formation-Active Galactic Nucleus Connection: Do All Star-forming Galaxies Host an Active Galactic Nucleus? *Astrophys. J.*, 782:9, 2014. [arXiv:1306.3218](#).
- [57] DiPompeo, M. A., A. D. Myers, R. C. Hickox, et al. The angular clustering of infrared-selected obscured and unobscured quasars. *Mon. Not. Roy. Astron. Soc.*, 442:3443–3453, 2014. [arXiv:1406.0778](#).
- [58] DiPompeo, M. A., A. D. Myers, R. C. Hickox, et al. Weighing obscured and unobscured quasar hosts with the cosmic microwave background. *Mon. Not. Roy. Astron. Soc.*, 446:3492–3501, 2015. [arXiv:1411.0527](#).
- [59] DiPompeo, M. A., J. C. Runnoe, R. C. Hickox, et al. The impact of the dusty torus on obscured quasar halo mass measurements. *Mon. Not. Roy. Astron. Soc.*, 460:175–186, 2016. [arXiv:1604.06811](#).
- [60] Mendez, A. J., A. L. Coil, J. Aird, et al. PRIMUS + DEEP2: Clustering of X-Ray, Radio, and IR-AGNs at $z \sim 0.7$. *Astrophys. J.*, 821:55, 2016. [arXiv:1504.06284](#).

- [61] Ross, A. J., S. Ho, A. J. Cuesta, et al. Ameliorating systematic uncertainties in the angular clustering of galaxies: a study using the SDSS-III. *Mon. Not. Roy. Astron. Soc.*, 417:1350–1373, 2011. [arXiv:1105.2320](#).
- [62] Ross, A. J., W. J. Percival, A. G. Sánchez, et al. The clustering of galaxies in the SDSS-III Baryon Oscillation Spectroscopic Survey: analysis of potential systematics. *Mon. Not. Roy. Astron. Soc.*, 424: 564–590, 2012. [arXiv:1203.6499](#).
- [63] Ross, A. J., F. Beutler, C.-H. Chuang, et al. The clustering of galaxies in the completed SDSS-III Baryon Oscillation Spectroscopic Survey: Observational systematics and baryon acoustic oscillations in the correlation function. *ArXiv e-prints*, 2016. [arXiv:1607.03145](#).
- [64] Myers, A. D., R. J. Brunner, G. T. Richards, et al. First Measurement of the Clustering Evolution of Photometrically Classified Quasars. *Astrophys. J.*, 638:622–634, 2006. [astro-ph/0510371](#).
- [65] Leistedt, B., H. V. Peiris, D. J. Mortlock, et al. Estimating the large-scale angular power spectrum in the presence of systematics: a case study of Sloan Digital Sky Survey quasars. *Mon. Not. Roy. Astron. Soc.*, 435:1857–1873, 2013. [arXiv:astro-ph.CO/1306.0005](#).
- [66] Leistedt, B. and H. V. Peiris. Exploiting the full potential of photometric quasar surveys: optimal power spectra through blind mitigation of systematics. *Mon. Not. Roy. Astron. Soc.*, 444:2–14, 2014. [arXiv:1404.6530](#).
- [67] Agarwal, N., S. Ho, A. D. Myers, et al. Characterizing unknown systematics in large scale structure surveys. *JCAP*, 4:007, 2014. [arXiv:1309.2954](#).
- [68] DiPompeo, M. A., R. C. Hickox, and A. D. Myers. Updated measurements of the dark matter halo masses of obscured quasars with improved WISE and Planck data. *Mon. Not. Roy. Astron. Soc.*, 456: 924–942, 2016. [arXiv:1511.04469](#).
- [69] Laurent, P., J.-M. Le Goff, E. Burtin, et al. A $14 h^{-3} \text{Gpc}^3$ study of cosmic homogeneity using BOSS DR12 quasar sample. *JCAP*, 11:060, 2016. [arXiv:1602.09010](#).
- [70] Eisenstein, D. J., D. H. Weinberg, E. Agol, et al. SDSS-III: Massive Spectroscopic Surveys of the Distant Universe, the Milky Way, and Extra-Solar Planetary Systems. *Astronom. J.*, 142:72, 2011. [arXiv:astro-ph.IM/1101.1529](#).
- [71] Anderson, L., E. Aubourg, S. Bailey, et al. The clustering of galaxies in the SDSS-III Baryon Oscillation Spectroscopic Survey: baryon acoustic oscillations in the Data Release 9 spectroscopic galaxy sample. *Mon. Not. Roy. Astron. Soc.*, 427:3435–3467, 2012. [arXiv:1203.6594](#).
- [72] Anderson, L., É. Aubourg, S. Bailey, et al. The clustering of galaxies in the SDSS-III Baryon Oscillation Spectroscopic Survey: baryon acoustic oscillations in the Data Releases 10 and 11 Galaxy samples. *Mon. Not. Roy. Astron. Soc.*, 441:24–62, 2014. [arXiv:1312.4877](#).
- [73] Anderson, L., E. Aubourg, S. Bailey, et al. The clustering of galaxies in the SDSS-III Baryon Oscillation Spectroscopic Survey: measuring D_A and H at $z = 0.57$ from the baryon acoustic peak in the Data Release 9 spectroscopic Galaxy sample. *Mon. Not. Roy. Astron. Soc.*, 439:83–101, 2014. [arXiv:astro-ph.CO/1303.4666](#).
- [74] Slosar, A., A. Font-Ribera, M. M. Pieri, et al. The Lyman- α forest in three dimensions: measurements of large scale flux correlations from BOSS 1st-year data. *JCAP*, 9:001, 2011. [arXiv:1104.5244](#).
- [75] Slosar, A., V. Iršič, D. Kirkby, et al. Measurement of baryon acoustic oscillations in the Lyman- α forest fluctuations in BOSS data release 9. *JCAP*, 4:026, 2013. [arXiv:1301.3459](#).
- [76] Busca, N. G., T. Delubac, J. Rich, et al. Baryon acoustic oscillations in the Ly α forest of BOSS quasars. *Astron. and Astrophys.*, 552:A96, 2013. [arXiv:astro-ph.CO/1211.2616](#).
- [77] Font-Ribera, A., D. Kirkby, N. Busca, et al. Quasar-Lyman α forest cross-correlation from BOSS DR11: Baryon Acoustic Oscillations. *JCAP*, 5:027, 2014. [arXiv:1311.1767](#).

- [78] Delubac, T., J. E. Bautista, N. G. Busca, et al. Baryon acoustic oscillations in the Ly α forest of BOSS DR11 quasars. *Astron. and Astrophys.*, 574:A59, 2015. [arXiv:1404.1801](#).
- [79] Zhao, G.-B., Y. Wang, A. J. Ross, et al. The extended Baryon Oscillation Spectroscopic Survey: a cosmological forecast. *Mon. Not. Roy. Astron. Soc.*, 457:2377–2390, 2016. [arXiv:1510.08216](#).
- [80] Prakash, A., T. C. Licquia, J. A. Newman, et al. The SDSS-IV Extended Baryon Oscillation Spectroscopic Survey: Luminous Red Galaxy Target Selection. *Astrophys. J. Suppl.*, 224:34, 2016. [arXiv:1508.04478](#).
- [81] Comparat, J., T. Delubac, S. Jovel, et al. SDSS-IV eBOSS emission-line galaxy pilot survey. *ArXiv e-prints*, 2015. [arXiv:1509.05045](#).
- [82] Raichoor, A., J. Comparat, T. Delubac, et al. The SDSS-IV extended Baryon Oscillation Spectroscopic Survey: selecting emission line galaxies using the Fisher discriminant. *Astron. and Astrophys.*, 585:A50, 2016. [arXiv:1505.01797](#).
- [83] Myers, A. D., N. Palanque-Delabrouille, A. Prakash, et al. The SDSS-IV Extended Baryon Oscillation Spectroscopic Survey: Quasar Target Selection. *Astrophys. J. Suppl.*, 221:27, 2015. [arXiv:1508.04472](#).
- [84] Palanque-Delabrouille, N., C. Magneville, C. Yèche, et al. The extended Baryon Oscillation Spectroscopic Survey: Variability selection and quasar luminosity function. *Astron. and Astrophys.*, 587:A41, 2016. [arXiv:1509.05607](#).
- [85] Rodríguez-Torres, S. A., J. Comparat, F. Prada, et al. Clustering of quasars in the First Year of the SDSS-IV eBOSS survey: Interpretation and halo occupation distribution. *ArXiv e-prints*, 2016. [arXiv:1612.06918](#).
- [86] Smee, S. A., J. E. Gunn, A. Uomoto, et al. The Multi-object, Fiber-fed Spectrographs for the Sloan Digital Sky Survey and the Baryon Oscillation Spectroscopic Survey. *Astronom. J.*, 146:32, 2013. [arXiv:1208.2233](#).
- [87] Gunn, J. E., W. A. Siegmund, E. J. Mannery, et al. The 2.5 m Telescope of the Sloan Digital Sky Survey. *Astronom. J.*, 131:2332–2359, 2006. [astro-ph/0602326](#).
- [88] Bovy, J., D. W. Hogg, and S. T. Roweis. Extreme deconvolution: Inferring complete distribution functions from noisy, heterogeneous and incomplete observations. *AOAS*, 5:1657, 2009. [arXiv:0905.2979](#).
- [89] Bovy, J., J. F. Hennawi, D. W. Hogg, et al. Think Outside the Color Box: Probabilistic Target Selection and the SDSS-XDQSO Quasar Targeting Catalog. *Astrophys. J.*, 729:141, 2011. [arXiv:1011.6392](#).
- [90] Bovy, J., A. D. Myers, J. F. Hennawi, et al. Photometric Redshifts and Quasar Probabilities from a Single, Data-driven Generative Model. *Astrophys. J.*, 749:41, 2012. [arXiv:1105.3975](#).
- [91] Fukugita, M., T. Ichikawa, J. E. Gunn, et al. The Sloan Digital Sky Survey Photometric System. *Astronom. J.*, 111:1748, 1996.
- [92] Finkbeiner, D. P., E. F. Schlafly, D. J. Schlegel, et al. Hypercalibration: A Pan-STARRS1-based Recalibration of the Sloan Digital Sky Survey Photometry. *Astrophys. J.*, 822:66, 2016. [arXiv:astro-ph.IM/1512.01214](#).
- [93] Wright, E. L., P. R. M. Eisenhardt, A. K. Mainzer, et al. The Wide-field Infrared Survey Explorer (WISE): Mission Description and Initial On-orbit Performance. *Astronom. J.*, 140:1868–1881, 2010. [arXiv:astro-ph.IM/1008.0031](#).
- [94] Anderson, L., E. Aubourg, S. Bailey, et al. The clustering of galaxies in the SDSS-III Baryon Oscillation Spectroscopic Survey: baryon acoustic oscillations in the Data Release 9 spectroscopic galaxy sample. *Mon. Not. Roy. Astron. Soc.*, 427:3435–3467, 2012. [arXiv:1203.6594](#).

- [95] Bianchi, D. and W. J. Percival. Unbiased clustering estimation in the presence of missing observations. *ArXiv e-prints*, 2017. [arXiv:1703.02070](#).
- [96] Swanson, M. E. C., M. Tegmark, A. J. S. Hamilton, et al. Methods for rapidly processing angular masks of next-generation galaxy surveys. *Mon. Not. Roy. Astron. Soc.*, 387:1391–1402, 2008. [arXiv:0711.4352](#).
- [97] Landy, S. D. and A. S. Szalay. Bias and variance of angular correlation functions. *Astrophys. J.*, 412: 64–71, 1993.
- [98] White, M., J. L. Tinker, and C. K. McBride. Mock galaxy catalogues using the quick particle mesh method. *Mon. Not. Roy. Astron. Soc.*, 437:2594–2606, 2014. [arXiv:1309.5532](#).
- [99] Pâris, I., P. Petitjean, N. P. Ross, et al. The Sloan Digital Sky Survey Quasar Catalog: twelfth data release. *ArXiv e-prints*, 2016. [arXiv:1608.06483](#).
- [100] Lewis, A., A. Challinor, and A. Lasenby. Efficient Computation of Cosmic Microwave Background Anisotropies in Closed Friedmann-Robertson-Walker Models. *Astrophys. J.*, 538:473–476, 2000. [astro-ph/9911177](#).
- [101] Smith, R. E., J. A. Peacock, A. Jenkins, et al. Stable clustering, the halo model and non-linear cosmological power spectra. *Mon. Not. Roy. Astron. Soc.*, 341:1311–1332, 2003. [astro-ph/0207664](#).
- [102] Kaiser, N. Clustering in real space and in redshift space. *Mon. Not. Roy. Astron. Soc.*, 227:1–21, 1987.
- [103] James, F. MINUIT Function Minimization and Error Analysis: Reference Manual Version 94.1. 1994.
- [104] Martini, P. and D. H. Weinberg. Quasar Clustering and the Lifetime of Quasars. *Astrophys. J.*, 547: 12–26, 2001. [astro-ph/0002384](#).
- [105] Kaiser, N. On the spatial correlations of Abell clusters. *Astrophys. J. Lett.*, 284:L9–L12, 1984.
- [106] Tinker, J. L., B. E. Robertson, A. V. Kravtsov, et al. The Large-scale Bias of Dark Matter Halos: Numerical Calibration and Model Tests. *Astrophys. J.*, 724:878–886, 2010. [arXiv:astro-ph.CO/1001.3162](#).
- [107] Cole, S. and N. Kaiser. Biased clustering in the cold dark matter cosmogony. *Mon. Not. Roy. Astron. Soc.*, 237:1127–1146, 1989.
- [108] Haiman, Z. and L. Hui. Constraining the Lifetime of Quasars from Their Spatial Clustering. *Astrophys. J.*, 547:27–38, 2001. [astro-ph/0002190](#).
- [109] Wyithe, J. S. B. and A. Loeb. Calibrating the Galaxy Halo-Black Hole Relation Based on the Clustering of Quasars. *Astrophys. J.*, 621:95–103, 2005. [astro-ph/0403714](#).
- [110] Tinker, J., A. V. Kravtsov, A. Klypin, et al. Toward a Halo Mass Function for Precision Cosmology: The Limits of Universality. *Astrophys. J.*, 688:709–728, 2008. [arXiv:0803.2706](#).
- [111] Croom, S. M., R. J. Smith, B. J. Boyle, et al. The 2dF QSO Redshift Survey - XII. The spectroscopic catalogue and luminosity function. *Mon. Not. Roy. Astron. Soc.*, 349:1397–1418, 2004. [arXiv:astro-ph/0403040](#).
- [112] Croom, S. M., B. J. Boyle, T. Shanks, et al. The 2dF QSO Redshift Survey - XIV. Structure and evolution from the two-point correlation function. *Mon. Not. Roy. Astron. Soc.*, 356:415–438, 2005. [astro-ph/0409314](#).
- [113] Schneider, D. P., P. B. Hall, G. T. Richards, et al. The Sloan Digital Sky Survey Quasar Catalog. IV. Fifth Data Release. *Astronom. J.*, 134:102–117, 2007. [arXiv:0704.0806](#).
- [114] Ross, N. P., Y. Shen, M. A. Strauss, et al. Clustering of Low-redshift ($z \leq 2.2$) Quasars from the Sloan Digital Sky Survey. *Astrophys. J.*, 697:1634–1655, 2009. [arXiv:astro-ph.CO/0903.3230](#).
- [115] Font-Ribera, A., E. Arnau, J. Miralda-Escudé, et al. The large-scale quasar-Lyman α forest cross-correlation from BOSS. *JCAP*, 5:18, 2013. [arXiv:astro-ph.CO/1303.1937](#).

- [116] Hopkins, P. F., A. Lidz, L. Hernquist, et al. The Co-Formation of Spheroids and Quasars Traced in their Clustering. *Astrophys. J.*, 662:110–130, 2007. [astro-ph/0611792](#).
- [117] Richards, G. T., M. A. Strauss, X. Fan, et al. The Sloan Digital Sky Survey Quasar Survey: Quasar Luminosity Function from Data Release 3. *Astronom. J.*, 131:2766–2787, 2006. [astro-ph/0601434](#).
- [118] Shankar, F., D. H. Weinberg, and J. Miralda-Escudé. Self-Consistent Models of the AGN and Black Hole Populations: Duty Cycles, Accretion Rates, and the Mean Radiative Efficiency. *Astrophys. J.*, 690:20–41, 2009. [arXiv:0710.4488](#).
- [119] Shen, Y., C. K. McBride, M. White, et al. Cross-correlation of SDSS DR7 Quasars and DR10 BOSS Galaxies: The Weak Luminosity Dependence of Quasar Clustering at $z \sim 0.5$. *Astrophys. J.*, 778:98, 2013. [arXiv:1212.4526](#).
- [120] Krolewski, A. G. and D. J. Eisenstein. Measuring the Luminosity and Virial Black Hole Mass Dependence of Quasar-Galaxy Clustering At $z \sim 0.8$. *Astrophys. J.*, 803:4, 2015. [arXiv:1501.03898](#).